Evaluating Muscle Fiber Contractility and the Transcriptome, Proteome, Metabolome, and Lipidome of the mdx/mTR Mouse Model of Duchenne Muscular Dystrophy

Douglas W Van Pelt[1], Yalda A Kharaz[2], Dylan C Sarver[3], Logan R Eckhardt[3], Justin T Dzierzawski[3], Nathaniel P Disser[4], Alex N Piacentini[4], Eithne Comerford[2], Brian McDonagh[5], Christopher L Mendias[3,4,6,*]

[1]Department of Rehabilitation Sciences, College of Health Sciences, University of Kentucky, Lexington, KY, USA

[2]Department of Musculoskeletal Biology, Institute of Ageing and Chronic Disease, University of Liverpool, Liverpool, UK

[3]Department of Orthopaedic Surgery, University of Michigan Medical School, Ann Arbor, MI, USA

[4]Hospital for Special Surgery, New York, NY, USA

[5]Department of Physiology, School of Medicine, National University of Ireland, Galway, Ireland

[6]Department of Physiology & Biophysics, Weill Cornell Medical College, New York, NY USA

*Corresponding author
Christopher Mendias, PhD
Hospital for Special Surgery
535 E 70th St
New York, NY 10021
USA
+1 212-606-1785 office
+1 212-249-2373 fax
mendiasc@hss.edu

Abstract

Duchenne muscular dystrophy (DMD) is a progressive neuromuscular disease characterized by extensive muscle weakness and eventual complete tetraplegia. The mdx mouse strain, which lacks a functional dystrophin protein, is the most frequently used small animal model in dystrophy research, but has limited pathological changes compared to patients with DMD. The mdx/mTR mouse strain, that lacks functional dystrophin and has depleted pools of muscle stem cells, is an emerging model of DMD. Previous reports have identified accelerated degeneration in mdx/mTR mice compared to mdx mice, but mdx/mTR mice have not been as extensively phenotyped. Therefore, to gain a greater understanding of the pathological changes present the mdx/mTR strain, we measured contractility of muscle fibers, and evaluated changes in the transcriptome with RNA sequencing, and in the proteome, metabolome, and lipidome using untargeted mass spectroscopy. The hindlimb muscles of four month old male wild type (WT) C57Bl/6 and mdx/mTR mice were used for analysis. We found no differences in the contractility of permeabilized muscle fibers between WT and mdx/mTR mice, but did observe divergent changes in the transcriptome and proteome, and changes in markers of skeletal muscle substrate metabolism that are informative about pathological changes in DMD.

Introduction

Duchenne muscular dystrophy (DMD) is a rapidly progressing neuromuscular disease characterized by profound muscle weakness that leads to a near total loss of mobility, as well as other comorbidities that severely limit quality of life [1,2]. The dystrophin gene, which is defective in patients with DMD, encodes a protein that plays a central role in transmitting forces generated by myofibrils within muscle fibers out to the extracellular matrix (ECM) which surrounds the muscle cell. The lack of dystrophin causes membrane shearing and other structural damage to muscle cells, which then leads to inflammation, scar tissue formation, and an eventual loss of muscle fibers [3-5]. Although there have been numerous innovations in the treatment of patients with DMD that have provided some improvements in muscle function and extended lifespan, the additional years gained in lifespan are often spent in a tetraplegic state in which they are entirely dependent upon others for their care [1,2]. Therefore, there is substantial room for improvement in our ability to treat the loss of strength in patients with DMD.

Mouse models of disease can serve an important role in providing additional information about the etiology of disease processes and can also be useful to screen potential therapies prior to conducting clinical trials. The mdx mouse contains a premature stop codon in exon 23 of the dystrophin gene resulting in a loss of a functional dystrophin protein, and this strain is the most commonly used preclinical model for the study of DMD [6]. While mdx mice lack dystrophin, they have a generally mild limb muscle phenotype that does not mimic the pathological changes observed in patients with DMD [6]. This deficiency has limited the utility of this model, and led to the development of additional mouse models with a phenotype that more closely parallels the human disease [6]. One reason that mdx mice do not show the progressive loss in muscle quality that is observed in patients with DMD is due to species-specific differences in satellite cells, which are the myogenic stem cells responsible for regenerating injured fibers [7]. Although

dystrophin does play a role in self-renewal and proper asymmetric cell division [8], murine but not human satellite cells pools are thought to avoid depletion by inducing the expression of telomerase genes which restore telomere length that is severely shortened in response to proliferating throughout continued cycles of degeneration and regeneration [9]. To address this and improve the mdx model, a new line of mice was generated in the mdx background in which the telomerase RNA component (Terc) gene was deleted [9]. These genetically modified animals, referred to as mdx/mTR mice, display reduced satellite cell abundance and proliferative capacity, and a more pronounced muscle degenerative phenotype than mdx mice [9].

The mdx/mTR mouse model has been used in previous studies which have quantified whole muscle force production and other phenotypic changes [10], but the extent of our knowledge of pathological changes present in the mdx/mTR mouse model compared to other models of DMD are more limited. In particular, while mdx/mTR mice display reduced whole muscle force production [9], the mechanisms behind this loss in force production are not known. Additionally, changes to the metabolome or proteome of muscles from mdx/mTR mice have not been documented, as they have to some extent in other dystrophic models [11]. To our knowledge, no previous report has comprehensively evaluated the pathological changes in an animal model of DMD which integrated untargeted transcriptomics, proteomics, metabolomics, and lipidomics. Therefore, to gain a greater understanding of the pathological changes present in mdx/mTR mice, we measured contractility of single, permeabilized muscle fibers, and evaluated changes in the transcriptome, proteome, metabolome, and lipidome in 4 month old male mdx/mTR mice, and compared these results directly to age-matched male wild type (WT) C57Bl/6 mice, and indirectly to other reported dystrophic models and studies of DMD patients in the literature.

Results and Discussion

Overview

We first sought to evaluate pathological changes in the hindlimb muscles of 4 month old WT and mdx/mTR mice, as the function of these muscles is important in maintaining ambulation. This age was selected to correspond to the approximate period of time when DMD patients begin to markedly lose mobility, as pathological changes are apparent in the muscles of mdx/mTR mice at 2 months of age [9]. We also observed grossly reduced cage activity and lack of mobility beginning at 3 months of age in mdx/mTR mice. The muscles that were analyzed include the extensor digitorum longus (EDL), gastrocnemius (gastroc), plantaris, tibialis anterior (TA) and soleus. The EDL, gastroc, plantaris, and TA are composed of mostly fast (type II) muscle fibers, while the soleus has a mixed distribution of slow (type I) and fast fibers [12]. Although we used different muscles to minimize the number of animals required to conduct this study, there is a substantial amount of similarity in the transcriptome of EDL, gastroc, plantaris, and TA muscles [13], and we think that conclusions from one of these fast fibered muscle groups can be extended to other muscles with similar fiber type distributions.

To gain a comprehensive view of changes in the transcriptome and proteome of skeletal muscles of mdx/mTR mice compared to WT mice, we performed mRNA sequencing (RNAseq) using TA muscles, and untargeted mass spectrometry-based proteomics of plantaris muscles. The principal component (PC) analysis of transcriptome data demonstrate divergence between WT and mdx/mTR mice (Figure 1A). A total of 14064 transcripts were detected and met appropriate expression cut-off thresholds, with 1791 transcripts demonstrating at least a 1.5-fold increase in expression and $P<0.05$, and 665 transcripts were at least 1.5-fold downregulated and significantly different (Figure 1B, Supplemental Table S1). To further increase the number of proteins that were analyzed, we analyzed the supernatant of homogenized plantaris muscles, as

well as proteins extracted from the insoluble fraction. This resulted in the detection of 12 additional proteins, in addition to 83 proteins that were already detected in the soluble fraction. Similar to the transcriptome, PC analysis of the proteome of WT and mdx/mTR groups also demonstrated divergence (Figure 2A). Of the 1237 proteins detected, 460 proteins had at least a 1.5-fold increase in abundance and $P<0.05$, and 25 proteins were at least 1.5-fold downregulated and significantly different (Figure 2B, Supplemental Table S2). We then evaluated changes in the transcriptome compared with the proteome and identified 1119 proteins that also had transcripts that were detected in RNAseq (Figure 3A). Of these 1119 protein:transcript pairs, 53.3% (95% confidence interval, 50.3-56.2%) had a fold change that was in the similar direction, while 46.7% (95% confidence interval, 43.8-49.7%) had a fold change of protein that did not match the direction of the transcript (Figure 3A). This distribution was significantly different than a random 50% distribution (Figure 3A). We then identified genes and proteins that have important roles in protein synthesis and degradation (Figure 3B), muscle fiber contractility and cytoskeletal architecture (Figure 3C), ECM (Figure 3D), and metabolism (Figure 3E), which will be discussed in subsequent sections. Additionally, qPCR analysis of a select set of genes was performed, and we generally observed similar directions in fold change directions between qPCR and RNAseq data (Table 1).

Muscle Mass, Fiber Contractility, and the Extracellular Matrix

The mass of muscles was greater in mdx/mTR mice, demonstrating an increase from 23% in EDL muscles to 45% in TA muscles (Figure 4A), which is generally similar to previous reports of mdx mice [14]. This elevated muscle mass was disproportionate to the 9% higher body mass of mdx/mTR mice (26.0±1.7g for WT, 28.3±0.9g for mdx/mTR, $P=0.02$). While we did not observe differences between wild type and mdx/mTR mice in terms of muscle fiber cross-

sectional area (CSA), the majority of muscle fibers of mdx/mTR mice contained centrally located nuclei, and fibrotic lesions were also noted (Figures 4B-D). This suggests that the increased mass of muscles of mdx/mTR mice is likely due to inflammation and an expansion of fibrotic ECM. This is supported by several findings from the RNAseq and proteomics data (Figure 3B). The major skeletal muscle calpains, μ-calpain (Capn1) and m-calpain (Capn2) were elevated in mdx/mTR muscles, along with cathepsin B (Ctsb) (Figure 3B). While the skeletal muscle specific E3 ubiquitin ligases MUSA1 (Fbxo30), atrogin-1 (Fbxo32), and MuRF-1 (Trim63) were not upregulated, although the 20S proteasome subunit Psmb5 was upregulated, and signaling molecules that induce the activation of the ubiquitin ligase system, activin A (Inhba), activin B (Inhbb), and TGFβ (Tgfb1) were upregulated (Figure 3B). Several proteins or genes involved with translation were upregulated, including Eef1a1, Eif4a1, Rpl14, and Rps26 (Figure 3A). These findings suggest that the muscles of mdx/mTR muscles are primed to synthesize new proteins to maintain muscle function, even though the cells continue to be damaged.

We next sought to evaluate muscle contractility. Previous studies in the EDL of 6-month old mdx mice demonstrated no difference in whole muscle maximum isometric force, but specific force, which is maximum isometric force normalized to muscle cross-sectional area (CSA), was reduced by 13% in mdx mice compared to WT controls [14]. Further, when EDL muscles from mdx mice are subjected to a lengthening contraction-induced injury in which the muscle is suddenly lengthened while maximally activated, mdx mice experience a two-fold greater force deficit than WT mice, indicating greater damage to contractile elements of muscle fibers [15]. However, at the single muscle fiber level, when comparing WT to mdx fibers there was no difference in maximum isometric force, specific force, or the force deficit in response to lengthening-contraction injury [16]. The lack of any appreciable difference in the susceptibility of

fibers from WT and mdx mice to injury was thought to occur as a result of the permeabilization disrupting the presence of dystrophin at the sarcolemma, although this was not directly addressed in the manuscript [16]. We are unaware of any studies that have directly assessed the contractility of muscle fibers from DMD patients, but specific force values from a limited case series of patients with milder forms of muscular dystrophy appear generally to be lower than healthy controls [17-19]. With this in mind, and because the specific force of intact lateral gastroc muscles from mdx/mTR mice was approximately 3.5-fold lower than WT mice [9] which is substantially greater than observations from mdx mice, we anticipated observing reductions in single fiber force production in mdx/mTR mice. However, there were no difference in the CSAs of permeabilized fibers, nor in maximum isometric force, specific force, or contraction-induced force deficits between wild type and mdx/mTR mice (Figure 5A-D). We then wanted to determine whether dystrophin was properly expressed at the sarcolemma, or if it was lost during the fiber permeabilization and isolation process. We performed a western blot for dystrophin in homogenates of approximately 30 permeabilized fibers pulled from bundles, and observed the presence of dystrophin in wild type muscles in western blots (Figure 5E). This was followed up by histology of permeabilized fibers demonstrating clear signal for dystrophin at the sarcolemma in wild type fibers, and as expected no signal was observed for fibers from mdx/mTR mice (Figure 5F). The typical myofibril striation pattern was maintained in mdx/mTR mice, supporting the contractile properties data, despite no pattern clearly demonstrating synthesis of sarcomere components such as α-actinin (Acta1), desmin (Des), moesin (Msn), myosin binding protein C (Mybpc2), myomesin (Myom1), myotilin (Myot), myozenin (Myoz1), myopalladin (Mypn), obscurin (Obscn), talin (Tln1), and the troponins (Tnn) (Figure 3C). For the myosin heavy chains, embryonic myosin heavy chain (Myh3) and perinatal myosin heavy chain (Myh8), which are expressed in regenerating fibers, were upregulated at the transcript level (Figure 3C).

Additionally, while subsarcolemmal nuclei were present as expected in both WT and mdx/mTR mice, we also frequently observed collections of several nuclei immediately adjacent to each other and in a central location of the fiber (Figure 5F), consistent with a recent injury and myotube fusion event. This is supported by upregulation in the myoblast fusion protein myomaker (Tmem8c) and the membrane patching protein dysferlin (Dysf) (Figure 3C), which are also important in membrane repair in other models of DMD [20,21].

Overall, the lack of a difference between permeabilized fiber contractility of WT and mdx/mTR mice in the current study is consistent with previous findings in mdx mice [16]. Although we expected to find altered force values at the single fiber level based on previously reported whole muscle data, whole muscle data was collected through direct nerve stimulation, and denervation and reduced EMG signal amplitude has been reported in mdx/mTR mice and in patients with DMD [22,23], which may result in reduced muscle activation and lower measured whole muscle forces. Additionally, by demonstrating that dystrophin remains at the sarcolemma in fibers of WT mice subjected to permeabilization, our findings support the notion that dystrophin plays little to no role in longitudinal force transmission within a muscle fiber. There is a clear role for dystrophin in the lateral transmission of force between fibers [24], and being able to transmit forces laterally between fibers also protects individual fibers from damage by distributing strain more evenly across fibers in a given muscle [25]. In the absence of dystrophin, the ability to distribute strain across fibers in a muscle is lost, which likely explains why mdx mice display greater force deficits as a result of whole muscle lengthening contraction induced injuries [15], but there is no deficits at the single fiber level when force is nearly entirely transmitted longitudinally.

There were also pathological changes noted in the muscle ECM of mdx/mTR mice. In support of a fibrotic response, the muscle fibroblast markers PDGFRa and FSP1 (S100a4) were

upregulated. There was an induction with nearly every gene that encodes an ECM-related protein, although there was some divergence between RNAseq and protein values (Figure 3D). Numerous proteoglycans such as biglycan (Bgn), decorin (Dcn), lumican (Lum), osteopontin (Spp1), tenascin C (Tnc), tenascin X (Tnxb), versican (Vcan), vinculin (Vcl), and vimentin (Vim) were upregulated at the transcript or protein level (Figure 3D), which is consistent with previous findings in 3 month old mdx and 6 month old mdx^{4cv} animals [26,27]. However, type Iα1 and type Iα2 collagen had a lower abundance in mdx/mTR muscles, while type VIα1 collagen protein was not different despite having an elevation in transcript (Figure 3D). In 6 month old mdx^{4cv} animals, which are thought to have a more severe muscle phenotype from the original strain of mdx mice, an elevation in type Iα1 and type VIα1 collagen protein was observed [27]. It is possible that the differences between these results in collagen changes are due to an earlier degenerative stage of the mdx/mTR mice, prior to the onset of more severe fibrosis. Indeed, as fibrillar collagens play a role in longitudinal force transmission, and many proteoglycans assist in organizing the extracellular space that is linked with the dystrophin associated glycoprotein complexes [28], it is possible that the induction in proteoglycans occurs due to the repeated cycles of fiber damage and remodeling. Additionally, an elevation in the matrix metalloproteinases MMP-2, -3, and -14 was also observed, and these may be degrading fibrillar and basal lamina collagens (Figure 3D).

Overall, based on the observations in this study and previous reports, while there are pathological changes to muscle fibers and the ECM apparent in histology, these changes do not appear to disrupt the intrinsic force generating capacity of muscle fibers. However these changes likely disrupt lateral force transmission throughout the muscle ECM in mdx/mTR mice.

Metabolomics and Lipidomics

Much of the previous work that has explored metabolic alterations that occur in DMD animal models has focused on cardiac muscle [11], but some studies have been performed in skeletal muscle tissue. Some limited studies in human subjects demonstrated reduced succinate and branched chain amino acids, increased glucose, triglycerides and cholesterol, and no difference in creatine/phosphocreatine or phospholipids in muscle biopsies in patients with DMD compared to controls [29,30]. The muscles from golden retriever canines with a form of muscular dystrophy demonstrate reduced Krebs cycle intermediates compared to wild type animals [31] and similar reductions in oxidative capacity were also observed in the muscles of mdx mice [32]. In the current study, we detected 62 metabolites in an untargeted mass spectroscopy platform. PC analysis demonstrated moderate overlap between the WT and mdx/mTR metabolome (Figure 6A). We observed higher levels of metabolites involved with glycolysis in mdx/mTR mice, such as 6-phosphoglycerate (6PG), fructose-6-phosphate and glucose-6-phosphate (F6P+G6P), fructose bisphosphate (FBP), phosphorylated hexoses (hexose-P), and phosphoenolpyruvate (PEP), while the branched chain amino acid valine was not different (Figure 6A-B, Supplemental Table S3). Consistent with these changes in glycolytic metabolites, enzymes involved in glycolysis such as pyruvate kinase (Pkm) were upregulated, although no difference in aldolase A (Aldoa) was observed, and phosphoglycerate kinase 1 (Pgk1) and phosphorylase kinase (Phkb) were downregulated at the transcript level but protein abundance was not different (Figure 3E).

For Krebs cycle intermediates, no differences were observed between groups for acetyl-phosphate (Acetyl-P), citrate and isocitrate (CIT+ICIT), or succinate, although malate was elevated (Figure 6B). Aconitase (Aco2) was not different at the transcript or protein level, while citrate synthase (Cs) and succinate dehydrogenase A (Sdha) transcripts were downregulated but had no differences in protein abundance, and myoglobin (Mb) RNA and protein were reduced in

mdx/mTR muscles (Figure 3E). Additionally, neuronal nitric oxide synthase (nNOS or Nos1) is an enzyme located at the dystrophin glycoprotein complex that converts the amino acid L-arginine to citrulline, and is known to be disrupted in patients with DMD [28]. We observed a downregulation in nNOS gene expression (Figure 3E) along with an accumulation in L-arginine (Figure 6B), consistent with a functional deficit in nNOS activity in mdx/mTR mice. Overall, while glycolytic flux was reduced in mdx/mTR mice, differences in the Krebs cycle are less clear, and little changes in free amino acids were observed.

Finally, we analyzed the lipid content of muscles. PC analysis demonstrated a general dissimilarity between the lipidome of WT and mdx/mTR mice (Figure 7A). Of the 452 lipid species detected, there were 11 (2.4%) that were at least 1.5-fold elevated and significantly different in mdx/mTR muscles compared to WT, and 20 (4.4%) that were 1.5 fold lower and significantly different (Figure 7B, Supplemental Table S4). When analyzing lipid species by class instead of metabolite, ceramides (Cer), diglycerides (DG) and free fatty acids (FFA) were reduced in mdx/mTR muscles, with an elevation in phosphatidylglycerols (PG) and sphingomyelins (SM) (Figure 7C). These findings differ from a previous report of 3 month old mdx mice, which displayed an elevation of PC and PE, although both mdx and mdx/mTR mice did not have differences in PS abundance [33]. Most of the enzymes involved in lipid uptake and storage were reduced at the RNA and protein level, such as fatty acid translocase (Cd36), acyl co-A synthetases (Acsl1 and Acss1), diacylglycerol o-acyltransferase 2 (Dgat2), fatty acid binding protein 3 (Fabp3), hormone sensitive lipase (Lipe), and perilipin 5 (Plin5). Additionally, enzymes involved in fatty acid uptake into mitochondria, such as carnitine acylcarnitine translocase (Slc25a20), and carnitine palmitoyltransferase (Cpt1b) were downregulated. For genes involved in β-oxidation of fatty acyl Co-As within the mitochondria, the medium and very long-chain acyl Co-A dehydrogenases (Acadm and Acadvl) were downregulated. Enzymes

involved in the production of protaglandins and leukotrienes, such as leukotriene A4 hydrolase (Lta4h), and prostaglandin E synthase 2 and 3 (Ptges2 and Ptges3) were downregulated, although no difference in protein abundance was detected. Unlike glycolysis or Krebs cycle pathways, there is a clearer pattern present for lipid metabolism in mdx/mTR mice, with general signs that lipid oxidation capacity is likely reduced in this dystrophic mouse model.

Limitations

There are several limitations to this work. We only evaluated mice at a single time point, chosen to be informative about the disease progression, but mdx/mTR mice are known to continue to develop pathological changes as they age. It is possible that extending the analysis to a later time point would demonstrate reductions in muscle fiber force production. Our analysis focused largely on fast fibered muscles, and other than histology and muscle mass, we did not evaluate changes in slow-fibered muscles like the soleus. We also did not evaluate the diaphragm, which is the most severely injured muscle in mouse models of DMD. Changes in the mRNA transcriptome were studied, and we did not evaluate other types of RNAs that play a role in muscle degeneration and regeneration. Mitochondrial respiration or the ability to metabolize glucose, fatty acids, and other substrates were not measured in real time, and conclusions about metabolic changes are based on static RNA, protein, and metabolite measures. We also only evaluated males in this study, as DMD is X-linked, however heterozygous females are known to have some muscle pathologies and reduced physical function. Despite these limitations, we feel that this work makes an important contribution to our understanding of pathological changes that occur in the muscles of mdx/mTR mice, and identifies several area for future exploration.

Conclusions

In this study we performed a comprehensive evaluation of the muscle fiber contractile properties, and the transcriptome, proteome, metabolome, and lipidome in WT and mdx/mTR mice in an integrative manner. We provide additional support to the notion that dystrophin is not involved in the longitudinal transfer of force within muscle fibers, despite having a continued presence at the sarcolemma. Four months of age appears to be a time in the lifespan of mdx/mTR mice in which fibrotic changes to the ECM are limited, but important metabolic changes were noted. The findings of elevated glycolytic metabolism in mdx/mTR mice in this study may also be relevant to the emerging field of exercise prescription in patients with DMD. Since lengthening contractions are associated with muscle damage, rehabilitation programs are generally limited to isometric and shortening contractions [34]. As low intensity, shortening contractions are associated with causing aerobic adaptations to muscles, and increased aerobic capacity is correlated with overall improved metabolic health and reductions in disease burden [35], low intensity exercise interventions may help patients with DMD to improve their quality of life. Additionally, although there are limitations in the translatability of findings from mdx/mTR mice to patients, this model is likely to be useful in preclinical evaluation of potential therapeutic interventions in patients with DMD.

Methods

Animals. This study was approved by the University of Michigan IACUC (protocol PRO00006079). Mice were obtained from Jackson Labs (Bar Harbor, ME, USA) and housed under specific pathogen free conditions. Mice were allowed *ad libidum* access to food and water, but were fasted for four hours prior to harvest to minimize any impacts of acute food consumption on metabolomic measurements. We utilized male mdx/mTR^{G2} mice (referred to as mdx/mTR mice in this paper, Jackson Labs strain 023535) which are deficient for both the dystrophin and telomerase RNA component (Terc) genes [9]. Wild type male C57BL/6J mice (referred to as WT mice in this paper, Jackson Labs strain 000664), which is the same background of the mdx/mTR mice, were used as controls. DNA obtained from tail biopsies, and genotype of animals was verified by PCR analysis of following guidelines of Jackson Labs. At four months of age, mice were injected with sodium pentobarbital via an intraperitoneal route to obtain deep anesthesia, tissues were harvested and weighed, and animals were humanely euthanized by anesthetic overdose followed by cervical dislocation. The tissues collected from both hindlimbs included the extensor digitorum longus (EDL), used for single fiber testing and histology; gastrocnemius (gastroc) muscles, used for histology; plantaris muscles, used for proteomics; soleus muscles, used for histology; and tibialis anterior (TA) muscles used for metabolomics/lipidomics and RNAseq/gene expression. A total of N=6 mice were used from each genotype, for a total of N=12 mice in the study.

RNA Sequencing (RNAseq) and Gene Expression. RNA was isolated from TA muscles using a miRNEasy kit (Qiagen, Valencia, CA, USA). RNA quality was assessed using a TapeStation (Agilent, Santa Clara, CA, USA) and all samples had a RNA integrity number greater than 9.0. For each sample, 250ng total RNA was delivered to the University of Michigan Sequencing Core for mRNA sequencing (RNAseq) analysis. Sample concentrations were

normalized, cDNA pools were created for each sample and cDNAs were then subsequently tagged with a barcoded oligo adapter to allow for sample specific resolution. Sequencing was carried out using an Illumina HiSeq 4000 platform (Illumina, San Diego, CA, USA) with 50bp single end reads and an average of approximately 65 million reads per sample. Quality assessment and fold change calculations were performed in BaseSpace (Illumina). Sequencing data was quality checked using FastQC, aligned to the reference genome (mm10, UCSC, Santa Cruz, CA, USA) with the STAR software package, and differential expression based on fragments per kilobase of transcript per million mapped reads was performed using DESeq2. Genes with a base mean expression of at least 10 were used in analysis (a total of 14064 transcripts met this threshold).

For gene expression analysis, RNA was reversed transcribed into cDNA using iScript Reverse Transcription Supermix (Bio-Rad). Quantitative PCR (qPCR) was performed with cDNA in a CFX96 real-time thermal cycler (Bio-Rad) using iTaq Universal SYBR Green Supermix (Bio-Rad). Target gene expression was normalized to the housekeeping gene β2-microglobulin, and further normalized to WT samples using the $2^{-\Delta\Delta Ct}$ method. Primer sequences are provided in Supplemental Table S5.

Proteomics. Proteomics was performed as reported in previous studies [36-38] at the University of Liverpool Centre of Proteome Research. Protein extraction of plantaris muscles was performed by first extracting soluble proteins from the homogenization supernatant, followed by second protein extraction of the remaining insoluble pellet of the muscle. Soluble proteins were extracted by homogenizing tissue in 25mM ammonium bicarbonate and 10mM iodoacetamide, followed by centrifugation and removal of the supernatant. Then 100µg of soluble protein was further reduced and alkylated, and in solution trypsin digestion was performed. The remaining pellet was resuspended in 500µl of 4M Guanidine-HCl extraction

buffer (GnHCl), 65mM dithiothreitol, 50mM sodium acetate, pH 5.8 for 48 h at 4ºC with shaking. The samples were then centrifuged, the supernatant was removed, and 50µg of the soluble GnHCl fraction was subjected to in solution-trypsin digest on 10µl of resin (StrataClean, Agilent, Cheshire, UK) followed by reduction and alkylation. The digests from the isolated soluble proteins (5µL, corresponding to 2.5µg of peptides) and of those from GnHCl fraction (10µL, corresponding to 5 µg peptides) were loaded onto a spectrometer (Q-Exactive Quadrupole-Orbitrap, Thermo Scientific, Loughborough, UK) on a one hour gradient with an intersample 30 minute blank loaded.

Raw spectra were converted to mgf files using Proteome Discovery (Thermo Scientific, Loughborough, UK) and resulting files were searched against the UniProt mouse sequence database using a Mascot server (Matrix Science, London, UK). Search parameters used were: peptide mass tolerance, 10ppm; fragment mass tolerance, 0.01Da; +1,+2,+3 ions; missed cleavages 1; instrument type ESI-TRAP. Variable modifications included carbamidomethylation of cysteine residues and oxidation of methionine. Label free quantification was performed using PEAKS Studio software (BSI, Waterloo, ON, Canada). Proteins identified from the soluble and the insoluble fraction were combined for each group, and MetaboAnalyst 4.0 [39] was used to quantify differences between groups.

Whole Muscle Histology. EDL, gastroc, and soleus muscles were snap frozen in tragacanth gum and stored at -80ºC until use. Muscles were sectioned at a thickness of 10µm, fixed with 4% paraformaldehyde, and then incubated in 0.2% Triton-X 100. Sections were then stained with wheat germ agglutinin (WGA) conjugated to AlexaFluor 555 (Thermo Fisher, Waltham, MA, USA) to label the extracellular matrix, and DAPI (Sigma, Saint Louis, MO, USA) to identify nuclei. Images of stained sections were taken on a microscope (BX51,

Olympus, Waltham, MA, USA), and ImageJ (NIH, Bethesda, MD, USA) was used to quantify fiber CSAs and the percentage of muscle fibers with centrally located nuclei.

Muscle Fiber Contractility. The contractility of chemically permeabilized muscle fibers was performed as described [40,41]. Briefly, fiber bundles were dissected from the EDL muscle, placed in skinning solution for 30 min and then in storage solution for 16 h at 4°C, followed by storage at -80°C. On the day of contractility assessment, samples were thawed slowly on ice, and individual fibres were pulled from bundles using fine mirror-finished forceps. Fibers were then placed in a chamber containing relaxing solution and secured at one end to a servomotor (Aurora Scientific, Aurora, ON, Canada) and the other end to a force transducer (Aurora Scientific) using two ties of 10-0 monofilament nylon suture (Ashaway Line & Twine, Ashaway, RI, USA). A laser diffraction measurement system was used to adjust fiber length to obtain a sarcomere length of 2.5µm. Mean fiber CSA was calculated assuming an elliptical cross-section, with diameters obtained at five positions along the fiber from high-magnification images taken from top and side views. Maximum isometric force (F_o) was elicited by immersing the fiber in a high calcium activation solution. Specific maximum isometric force (sF_o) was calculated by dividing F_o by fiber CSA. The susceptibility of fibers to a lengthening contraction-induced injury was assessed by applying a single stretch to fully-activated fibers. The stretch was equivalent in amplitude to 30% of fiber length, and was applied at a constant velocity of 0.5 fiber lengths per second. After the stretch, fibers were immediately returned to their original length and allowed to generate force until a new steady-state level was reached. The difference between the pre- and post-stretch forces was used to calculate force deficit, expressed as a percentage of pre-stretch F_o. Eight to ten fast fibers were tested from each EDL muscle.

Muscle Fiber Western Blot. Western blots of permeabilized muscle fibers was performed to evaluate the presence of dystrophin in fibers from samples that were pulled from bundles of

WT and mdx/mTR muscles, as described above. Approximately 30 pulled fibers from each sample were homogenized in Laemmli's sample buffer (Bio-Rad, Hercules, CA, USA), boiled for 2 minutes, and loaded into 7.5% polyacrylamide gels (Bio-Rad), and subjected to electrophoretic separation. Proteins were transferred to 0.2µm nitrocellulose membranes (Bio-Rad) using a semi-dry transfer apparatus (Trans-Blot Turbo, Bio-Rad). Membranes were then blocked with 5% powdered milk, and incubated with polyclonal rabbit antibodies against dystrophin (ab15277, AbCam, Cambridge, MA, USA), and goat anti-rabbit antibodies conjugated to horse radish peroxidase (A16124, Thermo Fisher). Proteins were detected using enhanced chemiluminescence reagents (Clarity, Bio-Rad) and imaged in a chemiluminescent system (ChemiDoc MP, Bio-Rad). Following visualization of proteins, membranes were briefly stained with Coomassie (Bio-Rad) to verify similar protein loading between lanes.

Muscle Fiber Histology. To determine whether dystrophin persisted at the sarcolemma after permeabilization, fibers from WT and mdx/mTR samples were pulled from bundles that were prepared as described above, and subjected to histological processing using previously reported techniques [42]. Fibers were fixed in 2% glutaraldehyde (Electron Microscopy Sciences, Hatfield, PA, USA), rinsed, and then incubated with phalloidin conjugated to AlexaFluor 555 (Thermo Fisher) to identify actin, polyclonal rabbit antibodies against dystrophin (ab15277, AbCam), and DAPI (Sigma) to label nuclei. Goat anti-rabbit antibodies conjugated to AlexaFluor 647 (A21244, Thermo Fisher) were used to detect primary antibodies. Slides were imaged using a laser scanning confocal microscope (LSM 880, Zeiss, Thornwood, NY, USA).

Metabolomics and Lipidomics. The University of Michigan Metabolomics Core performed mass spectrometry-based shotgun lipidomics and metabolomics measurements from snap frozen, homogenized muscle samples as described [43,44]. For lipidomics, lipids were extracted from samples with a solvent mixture consisting of 2:2:2 (v/v/v)

methanol:dichloromethane:water mixture at room temperature after adding internal standard mixture. Once dried, the samples were resuspended in a solution containing 1:5:85 (v/v/v) acetonitrile:water:isopropanol and 10mM ammonium acetate. Samples were then subjected to liquid chromatrography-mass spectrometry (LC-MS), and MS peaks were matched in-silico with LipidBlast [45]. Quantification was performed by Multiquant software (AB-SCIEX, Framingham, MA, USA). One WT sample failed quality control and was excluded from analysis.

For metabolomics, metabolites were extracted from frozen muscle in a solvent mixture containing 8:1:1 methanol:chloroform:water (v/v/v). Metabolites were derivatized and analyzed with gas chromatography-MS [46]. Quantification of metabolites was performed using Masshunter Quantitative Analysis software (Agilent Technologies, Santa Clara, CA, USA).

MetaboAnalyst 4.0 [39] was used to perform detailed statistical analyses for lipidomics and metabolomics assays.

Statistics. Values are presented as mean±SD. Differences between groups were assessed using t-tests (α=0.05). For RNAseq, proteomics, lipidomics, and metabolomics data, a FDR-correction was applied to adjust for multiple observations. A binomial test (α=0.05) was used to compare the distribution of matched proteins and transcripts that have the same direction of fold change in mdx/mTR mice normalized to controls and in those which the direction of the fold change of the protein is different from the transcript. A Wilson/Brown approach was used to generate 95% confidence intervals for the percent distribution. With the exception of analyses performed in DESeq2 or MetaboAnalyst, statistical calculations were performed using Prism software (version 8.0, GraphPad, San Diego, CA, USA).

References

1. Ryder, S. *et al.* The burden, epidemiology, costs and treatment for Duchenne muscular dystrophy: an evidence review. *Orphanet J Rare Dis* **12,** 79 (2017).
2. Korinthenberg, R. A new era in the management of Duchenne muscular dystrophy. *Developmental medicine and child neurology* **61,** 292–297 (2019).
3. Claflin, D. R. & Brooks, S. V. Direct observation of failing fibers in muscles of dystrophic mice provides mechanistic insight into muscular dystrophy. *Am J Physiol, Cell Physiol* **294,** C651–8 (2008).
4. Kharraz, Y., Guerra, J., Pessina, P., Serrano, A. L. & Muñoz-Cánoves, P. Understanding the process of fibrosis in Duchenne muscular dystrophy. *Biomed Res Int* **2014,** 965631 (2014).
5. Petrof, B. J., Shrager, J. B., Stedman, H. H., Kelly, A. M. & Sweeney, H. L. Dystrophin protects the sarcolemma from stresses developed during muscle contraction. *Proc Natl Acad Sci USA* **90,** 3710–3714 (1993).
6. Ng, R. *et al.* Animal models of muscular dystrophy. *Prog Mol Biol Transl Sci* **105,** 83–111 (2012).
7. Gumucio, J. P., Sugg, K. B. & Mendias, C. L. TGF-β Superfamily Signaling in Muscle and Tendon Adaptation to Resistance Exercise. *Exerc Sport Sci Rev* **43,** 93–99 (2015).
8. Dumont, N. A. & Rudnicki, M. A. Targeting muscle stem cell intrinsic defects to treat Duchenne muscular dystrophy. *npj Regenerative Medicine* **1,** 291 (2016).
9. Sacco, A. *et al.* Short telomeres and stem cell exhaustion model Duchenne muscular dystrophy in mdx/mTR mice. *Cell* **143,** 1059–1071 (2010).
10. Yucel, N., Chang, A. C., Day, J. W., Rosenthal, N. & Blau, H. M. Humanizing the mdx mouse model of DMD: the long and the short of it. *npj Regenerative Medicine* **3,** 4 (2018).

11. Griffin, J. L. & Rosiers, Des, C. Applications of metabolomics and proteomics to the mdx mouse model of Duchenne muscular dystrophy: lessons from downstream of the transcriptome. *Genome Med* **1,** 32 (2009).

12. Burkholder, T. J., Fingado, B., Baron, S. & Lieber, R. L. Relationship between muscle fiber types and sizes and muscle architectural properties in the mouse hindlimb. *J Morphol* **221,** 177–190 (1994).

13. Terry, E. E. *et al.* Transcriptional profiling reveals extraordinary diversity among skeletal muscle tissues. *Elife* **7,** 1334 (2018).

14. Lynch, G. S., Hinkle, R. T., Chamberlain, J. S., Brooks, S. V. & Faulkner, J. A. Force and power output of fast and slow skeletal muscles from mdx mice 6-28 months old. *J Physiol (Lond)* **535,** 591–600 (2001).

15. Consolino, C. M. & Brooks, S. V. Susceptibility to sarcomere injury induced by single stretches of maximally activated muscles of mdx mice. *J Appl Physiol* **96,** 633–638 (2004).

16. Lynch, G. S., Rafael, J. A., Chamberlain, J. S. & Faulkner, J. A. Contraction-induced injury to single permeabilized muscle fibers from mdx, transgenic mdx, and control mice. *Am J Physiol, Cell Physiol* **279,** C1290–4 (2000).

17. Krivickas, L. S., Walsh, R. & Amato, A. A. Single muscle fiber contractile properties in adults with muscular dystrophy treated with MYO-029. *Muscle Nerve* **39,** 3–9 (2009).

18. Claflin, D. R. *et al.* Effects of high-and low-velocity resistance training on the contractile properties of skeletal muscle fibers from young and older humans. *J Appl Physiol* **111,** 1021–1030 (2011).

19. Mendias, C. L. *et al.* Reduced muscle fiber force production and disrupted myofibril architecture in patients with chronic rotator cuff tears. *J Shoulder Elbow Surg* **24,** 111–119 (2015).

20. Millay, D. P., Sutherland, L. B., Bassel-Duby, R. & Olson, E. N. Myomaker is essential for muscle regeneration. *Genes Dev* **28,** 1641–1646 (2014).

21. Wallace, G. Q. & McNally, E. M. Mechanisms of muscle degeneration, regeneration, and repair in the muscular dystrophies. *Annu Rev Physiol* **71,** 37–57 (2009).

22. Verma, S., Lin, J., Travers, C., McCracken, C. & Shah, D. Quantitative electromyography in ambulatory boys with Duchenne muscular dystrophy. *Muscle Nerve* **56,** 1168–1171 (2017).

23. Tierney, M., Garcia, C., Bancone, M., Sacco, A. & Personius, K. E. Innervation of dystrophic muscle after muscle stem cell therapy. *Muscle Nerve* **54,** 763–768 (2016).

24. Ramaswamy, K. S. *et al.* Lateral transmission of force is impaired in skeletal muscles of dystrophic mice and very old rats. *J Physiol (Lond)* **589,** 1195–1208 (2011).

25. Palmer, M. L., Claflin, D. R., Faulkner, J. A. & Panchangam, A. Non-uniform distribution of strain during stretch of relaxed skeletal muscle fibers from rat soleus muscle. *J Muscle Res Cell Motil* **32,** 39–48 (2011).

26. Murphy, S. *et al.* Proteomic profiling of the dystrophin complex and membrane fraction from dystrophic mdx muscle reveals decreases in the cytolinker desmoglein and increases in the extracellular matrix stabilizers biglycan and fibronectin. *J Muscle Res Cell Motil* **38,** 251–268 (2017).

27. Murphy, S. *et al.* Concurrent Label-Free Mass Spectrometric Analysis of Dystrophin Isoform Dp427 and the Myofibrosis Marker Collagen in Crude Extracts from mdx-4cv Skeletal Muscles. *Proteomes* **3,** 298–327 (2015).

28. Carmen, L. *et al.* Role of proteoglycans and glycosaminoglycans in Duchenne muscular dystrophy. *Glycobiology* **29,** 110–123 (2019).

29. Srivastava, N. K., Yadav, R., Mukherjee, S., Pal, L. & Sinha, N. Abnormal lipid metabolism in skeletal muscle tissue of patients with muscular dystrophy: In vitro, high-resolution NMR spectroscopy based observation in early phase of the disease. *Magn Reson Imaging* **38,** 163–173 (2017).

30. Srivastava, N. K., Yadav, R., Mukherjee, S. & Sinha, N. Perturbation of muscle metabolism in patients with muscular dystrophy in early or acute phase of disease: In vitro, high resolution NMR spectroscopy based analysis. *Clin. Chim. Acta* **478,** 171–181 (2018).

31. Abdullah, M. *et al.* Non-Targeted Metabolomics Analysis of Golden Retriever Muscular Dystrophy-Affected Muscles Reveals Alterations in Arginine and Proline Metabolism, and Elevations in Glutamic and Oleic Acid In Vivo. *Metabolites* **7,** (2017).

32. Even, P. C., Decrouy, A. & Chinet, A. Defective regulation of energy metabolism in mdx-mouse skeletal muscles. *Biochemical Journal* **304 (Pt 2),** 649–654 (1994).

33. Paran, C. W. *et al.* Lipogenesis mitigates dysregulated sarcoplasmic reticulum calcium uptake in muscular dystrophy. *Biochim Biophys Acta* **1851,** 1530–1538 (2015).

34. Kostek, M. C. & Gordon, B. Exercise Is an Adjuvant to Contemporary Dystrophy Treatments. *Exerc Sport Sci Rev* **46,** 34–41 (2018).

35. Koch, L. G. & Britton, S. L. Theoretical and Biological Evaluation of the Link between Low Exercise Capacity and Disease Risk. *Cold Spring Harb Perspect Med* **8,** a029868 (2018).

36. McDonagh, B., Sakellariou, G. K., Smith, N. T., Brownridge, P. & Jackson, M. J. Differential cysteine labeling and global label-free proteomics reveals an altered metabolic state in skeletal muscle aging. *J. Proteome Res.* **13,** 5008–5021 (2014).

37. Sarver, D. C. *et al.* Sex differences in tendon structure and function. *J Orthop Res* **35,** 2117–2126 (2017).

38. Ashraf Kharaz, Y. *et al.* Comparison between chaotropic and detergent-based sample preparation workflow in tendon for mass spectrometry analysis. *Proteomics* **17,** 1700018 (2017).

39. Chong, J. *et al.* MetaboAnalyst 4.0: towards more transparent and integrative metabolomics analysis. *Nucleic Acids Res* **46,** W486–W494 (2018).

40. Mendias, C. L., Kayupov, E., Bradley, J. R., Brooks, S. V. & Claflin, D. R. Decreased specific force and power production of muscle fibers from myostatin-deficient mice are associated with a suppression of protein degradation. *J Appl Physiol* **111,** 185–191 (2011).

41. Mendias, C. L. *et al.* Changes in skeletal muscle and tendon structure and function following genetic inactivation of myostatin in rats. *J Physiol (Lond)* **593,** 2037–2052 (2015).

42. Mackey, A. L. & Kjaer, M. The breaking and making of healthy adult human skeletal muscle in vivo. *Skelet Muscle* **7,** 24 (2017).

43. Sarver, D. C. *et al.* Local cryotherapy minimally impacts the metabolome and transcriptome of human skeletal muscle. *Sci Rep* **7,** 2423 (2017).

44. Gumucio, J. P. *et al.* Reduced mitochondrial lipid oxidation leads to fat accumulation in myosteatosis. doi:10.1101/471979

45. Kind, T. *et al.* LipidBlast in silico tandem mass spectrometry database for lipid identification. *Nat. Methods* **10,** 755–758 (2013).

46. Lorenz, M. A., Burant, C. F. & Kennedy, R. T. Reducing time and increasing sensitivity in sample preparation for adherent mammalian cell metabolomics. *Anal. Chem.* **83,** 3406–3414 (2011).

Acknowledgements

The authors would like to acknowledge technical contributions from Mr. Maxwell Konnaris and Mr. Patrick Zager at the Hospital for Special Surgery, and Dr. Deborah Simpson at the University of Liverpool. This work was supported by NIH grants R01-AR063649 and U24-DK097153.

Author Contributions

DVP, YAK, EC, BM, and CLM designed the study; DVP and CLM wrote the manuscript; DVP, YAK, DCS, LRE, JTD, NPD, ANP, BM, and CLM performed experiments; DVP, YAK, EC, BM, and CLM performed data analysis. All authors reviewed the manuscript.

Competing Interests

The authors declare they have no competing interests.

Data Availability

Mass spectrometry and gene expression data are available in Supplemental Tables. The proteomics data set for this study has been deposited in the ProteomeXchange Consortium via the PRIDE partner repository (accession PXD010507). RNAseq data has been deposited to NIH GEO (accession GSE127929). Any additional data is available from the corresponding author on reasonable request.

Figures

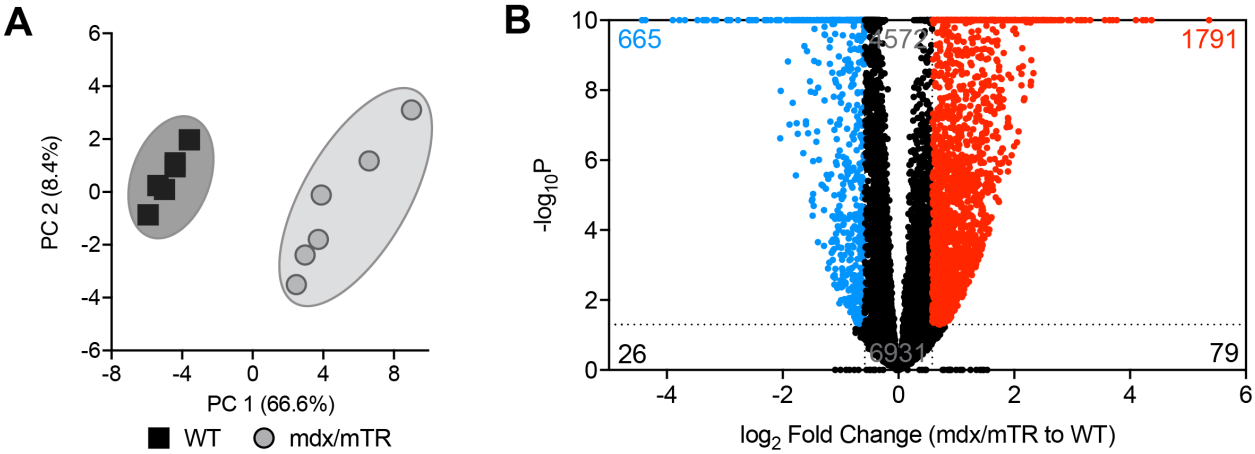

Figure 1. RNA sequencing. (A) Principal component (PC) analysis of RNA sequencing data. (B) Volcano plot demonstrating $\log_2$ fold-change and FDR-corrected P-values of all measured transcripts. Genes with $-\log_{10}P$ values greater than 10 are shown directly on the top border of the graph. Genes with a > 1.5-fold upregulation in mdx/mTR mice ($\log_2$ fold change > 0.585) and P value < 0.05 ($-\log_{10}P > 1.3$) are shown in red. Genes with a > 1.5-fold downregulation in mdx/mTR mice ($\log_2$ fold change < -0.585) and P value < 0.05 ($-\log_{10}P > 1.3$) are shown in blue. N=6 WT and N=6 mdx/mTR mice per group.

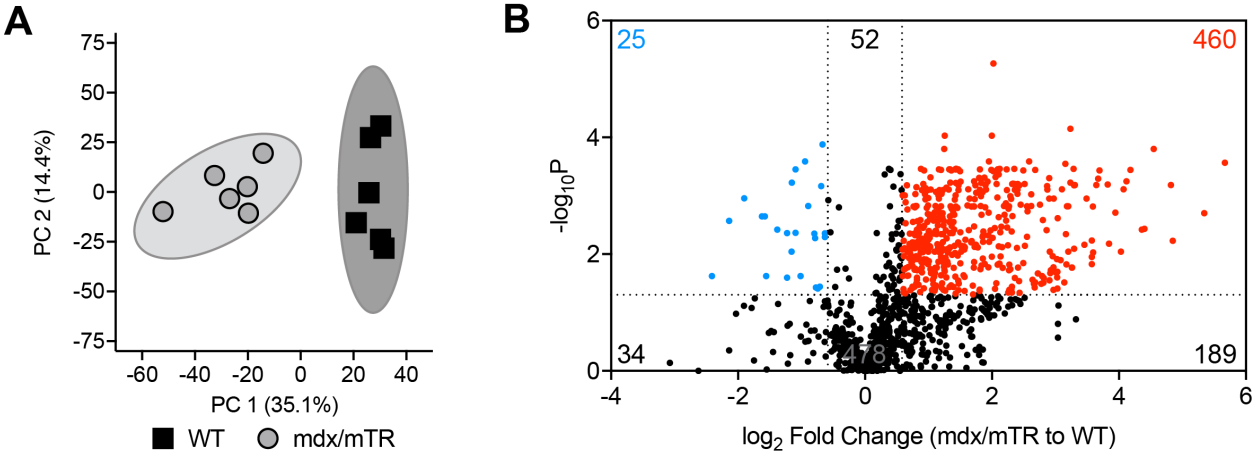

Figure 2. Proteomics. (A) Principal component (PC) analysis of proteomics data. (B) Volcano plot demonstrating $\log_2$ fold-change and FDR-corrected P-values of all measured proteins. Proteins with a > 1.5-fold increase in mdx/mTR mice ($\log_2$ fold change > 0.585) and P value < 0.05 ($-\log_{10}P > 1.3$) are shown in red. Genes with a > 1.5-fold decrease in mdx/mTR mice ($\log_2$ fold change < -0.585) and P value < 0.05 ($-\log_{10}P > 1.3$) are shown in blue. N=6 WT and N=6 mdx/mTR mice per group.

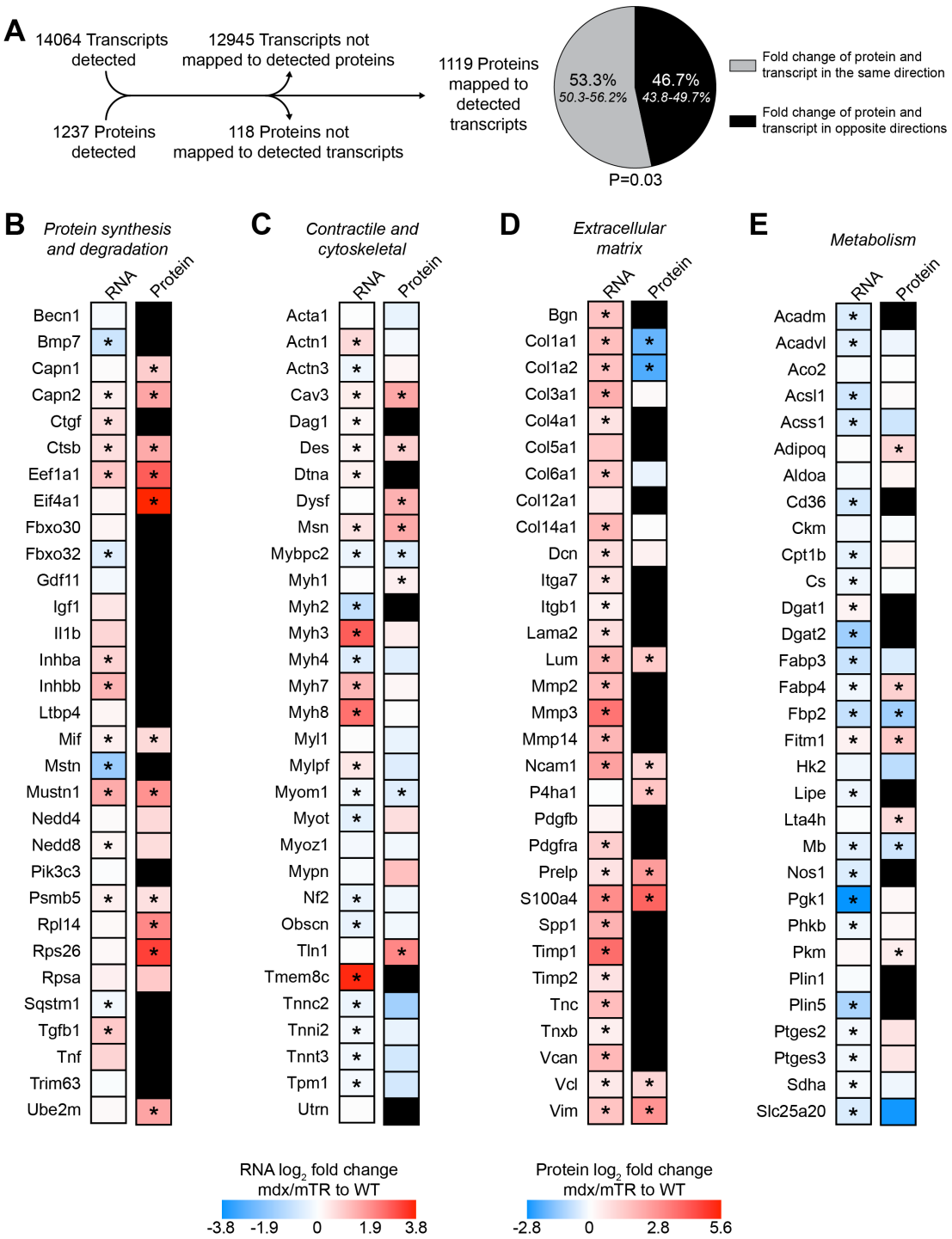

Figure 3. Integrated RNA sequencing and Proteomics. (A) Overview of the total number of transcripts and proteins detected, the number of proteins that matched to transcripts, and the percentage (with 95% confidence interval) of matched proteins and transcripts that have the same direction of fold change in mdx/mTR mice normalized to controls (gray), and those in which the direction of the fold change of the protein is different from the transcript (black). A binomial test was performed to compare the observed distribution to the expected distribution. Heatmap demonstrating the $\log_2$ fold change in selected genes and proteins related to (B) protein synthesis and degradation, (C) contractility and the cytoskeleton, (D) the extracellular matrix, and (E) metabolism. Black box indicates that the protein was not present in the proteomics data set. Differences between groups (B-E) assessed using t-tests; *, significantly different ($P<0.05$) from WT. N=6 WT and N=6 mdx/mTR mice.

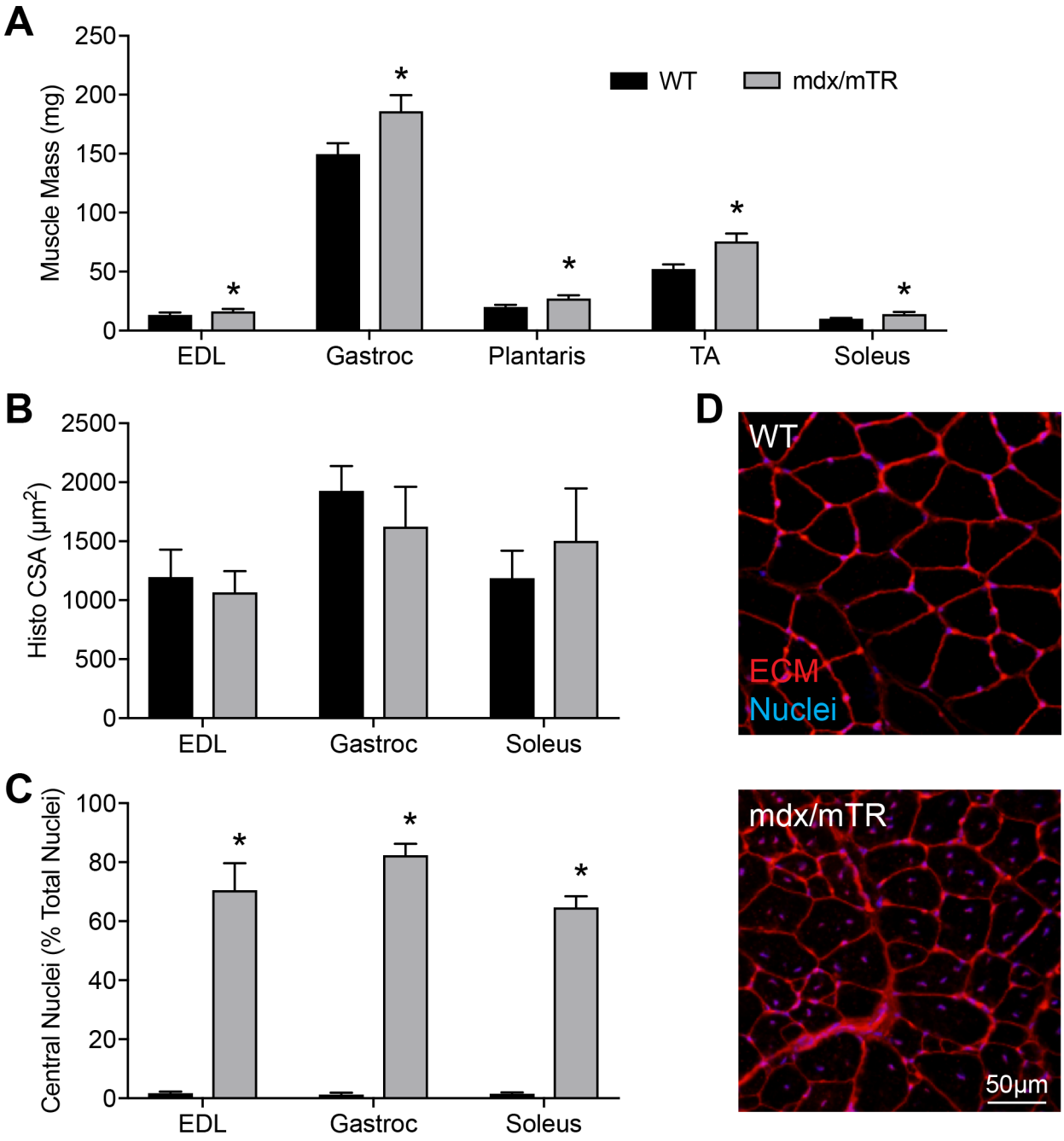

Figure 4. Muscle Mass and Histology. (A) Muscle mass data from extensor digitorum longus (EDL), gastrocnemius (gastroc), plantaris, tibialis anterior (TA) and soleus muscles. (B) Histological cross-sectional area (CSA) and (C) fibers that contain centrally located nuclei, expressed as a percentage of total fibers. (D) Representative histology from WT and mdx/mTR gastroc muscles; red, WGA-AF555/extracellular matrix; blue, DAPI/nuclei. Scale bar for both images is 50μm. Values are mean+SD, differences between groups assessed using t-tests; *, significantly different ($P<0.05$) from WT. N=6 WT and N=6 mdx/mTR mice.

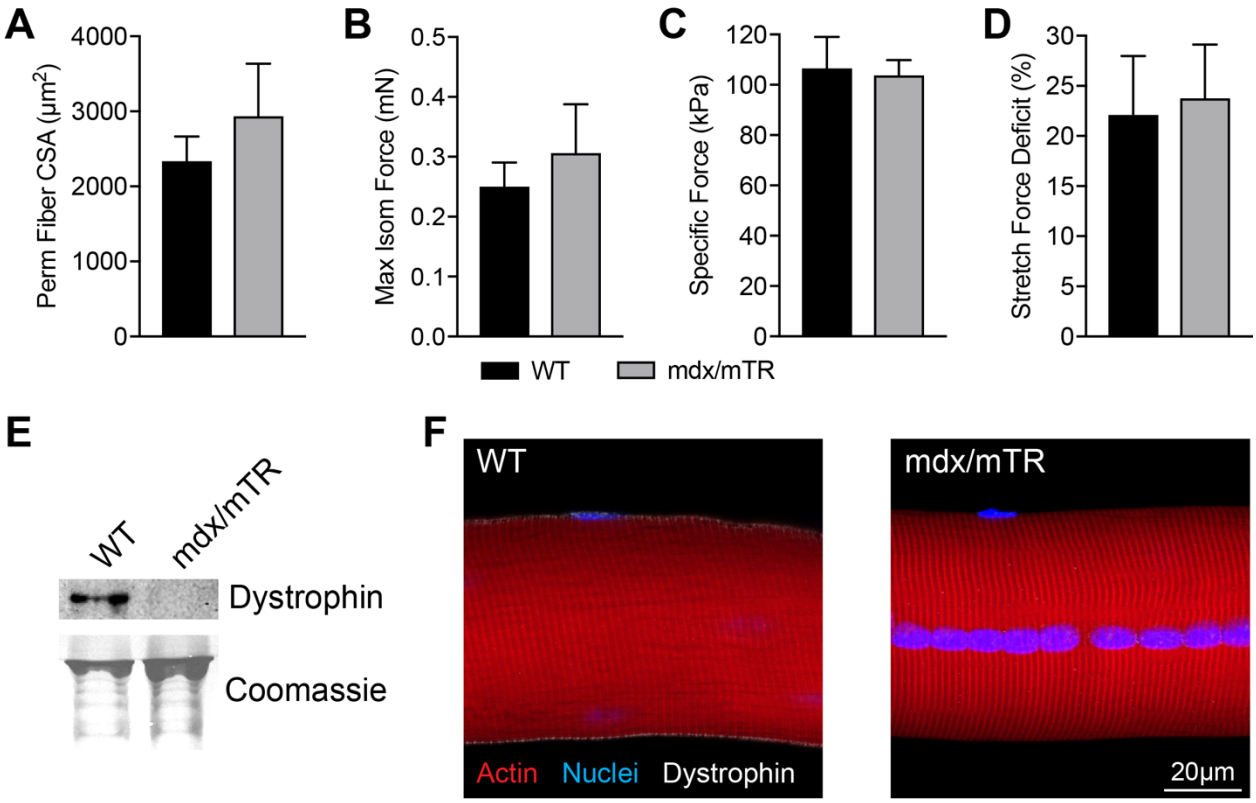

Figure 5. Permeabilized Extensor Digitorum Longus Muscle Fiber Force and Fiber Morphology. (A) Permeabilized fiber cross-sectional area (CSA), (B) maximum isometric force, (C) specific force, and (D) force deficit after active stretch induced injury. Values are mean+SD, differences between groups assessed using t-tests; no differences detected between WT and mdx/mTR groups. N=6 WT and N=6 mdx/mTR mice. (E) Western blot and (F) histology of permeabilized fibers demonstrating the presence of dystrophin at the sarcolemma of fibers after the permeabilization process; red, actin; blue, DAPI/nuclei; white, dystrophin. Scale bar in both images is 20μm.

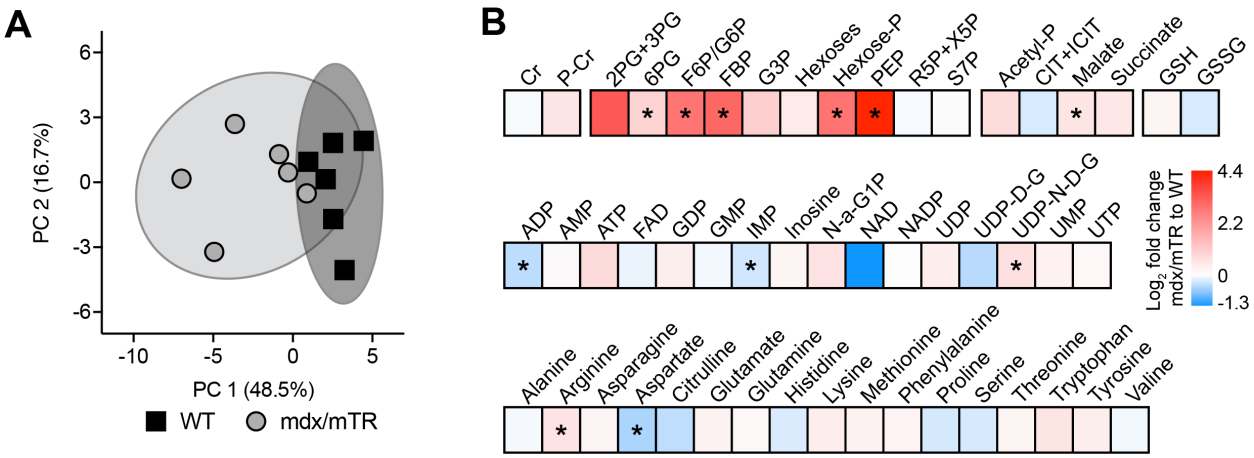

Figure 6. Metabolomics. (A) Principal component (PC) analysis of metabolomics data. (B) Heatmap demonstrating the $\log_2$ fold change in selected metabolites involved in the creatine phosphate shuttle, glycolysis, Krebs cycle, glutathione metabolism, nucleotide and nucleoside metabolism, as well as free amino acids: creatine (Cr), phospho-creatine (P-Cr), 2-phosphoglycerate and 3-phosphoglycerate (2PG+3PG), 6-phosphoglycerate (6PG), fructose-6-phosphate and glucose-6-phosphate (F6P+G6P), fructose bisphosphate (FBP), glyceraldehyde 3-phosphate (G3P), hexose-phosphates (Hexose-P), phosphoenolpyruvate (PEP), ribulose 5-phosphate and xylulose 5-phosphate (R5P+X5P), sedoheptulose 7-phosphate (S7P), acetyl-phosphate (Acetyl-P), citrate and isocitrate (CIT+ICIT), reduced glutathione (GSH), oxidized glutathione (GSSG), adenosine diphosphate (ADP), adenosine monophosphate (AMP), adenosine triphosphate (ATP), flavin adenine dinucleotide (FAD), guanosine diphosphate (GDP), guanosine monophosphate (GMP), inosine monophosphate (IMP), N-Acetyl-glucosamine-1-phosphate (N-A-G1P), nicotinamide adenine dinucleotide (NAD), nicotinamide adenine dinucleotide phosphate (NADP), uridine diphosphate (UDP), uridine diphosphate-D-glucose (UDP-D-G), uridine diphosphate-N-acetyl-D-glucosamine (UDP-N-D-G), uridine monophosphate (UMP), uridine triphosphate (UTP). Differences between groups assessed using t-tests; *, significantly different ($P<0.05$) from WT. N=6 WT and N=6 mdx/mTR mice.

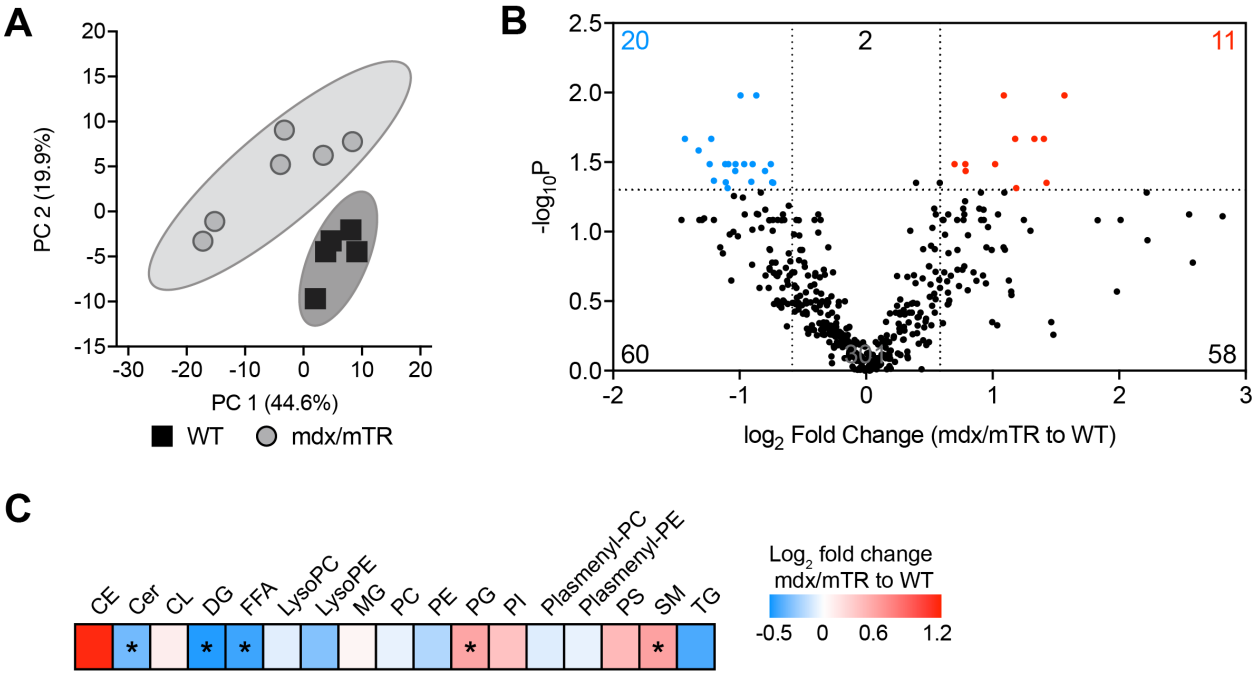

Figure 7. Lipidomics. (A) Principal component (PC) analysis of lipidomics data. (B) Volcano plot demonstrating fold-change and FDR-corrected P-values of all measured lipid species. Lipid species with a > 1.5-fold increase in mdx/mTR mice (log_2 fold change > 0.585) and P value < 0.05 ($-log_{10}P > 1.3$) are shown in red. Lipid species with a > 1.5-fold decrease in mdx/mTR mice (log_2 fold change < -0.585) and P value < 0.05 ($-log_{10}P > 1.3$) are shown in blue. (C) Heatmap demonstrating the log_2 fold change in classes of lipids: Cholesterol ester (CE), ceramides (Cer), cardiolipins (CL), diglycerides (DG), free fatty acids (FFA), lysophosphatidylcholines (LysoPC), lysophosphatidylethanolamines (LysoPE), monoglycerides (MG), phosphatidylcholines (PC), phosphatidylethanolamines (PE), phosphatidylglycerols (PG), phosphatidylinositols (PI), plasmenyl phosphatidylcholines (Plasmenyl-PC), plasmenyl phosphatidylethanolamines (Plasmenyl PE), phosphatidylserines (PS), sphingomyelins (SM), and triglycerides (TG). Differences between groups assessed using t-tests; *, significantly different (P<0.05) from WT. N=5 WT and N=6 mdx/mTR mice.

Table 1. Changes in gene expression as measured by qPCR. Gene expression values from tibialis anterior muscles. Values are mean±CV, differences tested between groups using t-tests; *, significantly different (P<0.05) from WT. N=6 WT and 6 mdx/mTR mice.

Gene	WT	mdx/mTR
Col1a1	1.00±0.47	2.19±1.09*
Col5a1	1.00±0.29	1.50±0.63
Dgat2	1.00±0.76	0.42±0.41
Fbxo32	1.00±0.88	0.72±0.57
Mmp14	1.00±0.35	2.00±0.95*
Mstn	1.00±0.52	0.38±0.23*
Myh8	1.00±0.50	35.9±25.0*
Tmem8c	1.00±0.44	16.7±8.30*